

## Anomalous Plastic Deformation and Sputtering of Ion Irradiated Silicon Nanowires

Andreas Johannes,<sup>\*,†</sup> Stefan Noack,<sup>†</sup> Werner Wesch,<sup>†</sup> Markus Glaser,<sup>‡</sup> Alois Lugstein,<sup>‡</sup> and Carsten Ronning<sup>†</sup>

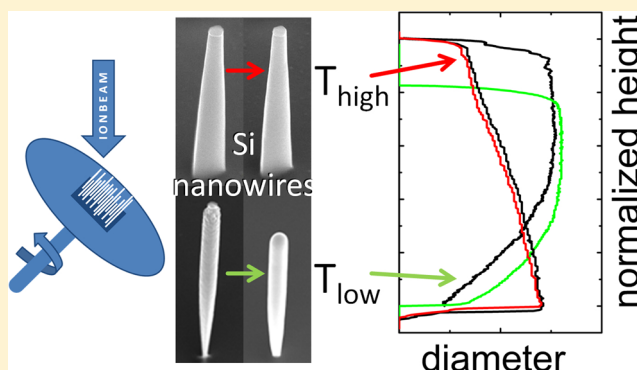
<sup>†</sup>Institute for Solid State Physics, Friedrich-Schiller-University Jena, Max-Wien-Platz 1, 07743, Jena, Germany

<sup>‡</sup>Institute of Solid State Electronics, Vienna University of Technology, Floragasse 7, 1040, Vienna, Austria

### S Supporting Information

**ABSTRACT:** Silicon nanowires of various diameters were irradiated with 100 keV and 300 keV Ar<sup>+</sup> ions on a rotatable and heatable stage. Irradiation at elevated temperatures above 300 °C retains the geometry of the nanostructure and sputtering can be gauged accurately. The diameter dependence of the sputtering shows a maximum if the ion range matches the nanowire diameter, which is in good agreement with Monte Carlo simulations based on binary collisions. Nanowires irradiated at room temperature, however, amorphize and deform plastically. So far, plastic deformation has not been observed in bulk silicon at such low ion energies. The magnitude and direction of the deformation is independent of the ion-beam direction and cannot be explained with mass-transport in a binary collision cascade but only by collective movement of atoms in the collision cascade with the given boundary conditions of a high surface to volume ratio.

**KEYWORDS:** Nanostructure, nanowire, thermal-spike, plastic deformation, silicon, ion irradiation, sputtering



Silicon is to date the most studied semiconductor and ion irradiation in silicon has been studied at great lengths, as it is instrumental in the development and production of modern microelectronics. Ion implantation is a versatile tool to modify the properties of semiconductors in general and Si specifically, and many textbooks cover the topic.<sup>1–4</sup> Also, the opportunities of nanostructured materials are manifold with new possible applications arising from a “simple” enhanced surface area for catalysts or sensors, via efficient wave-guiding of light for optoelectronics, to entirely new physical properties arising from quantum confinement. Many of these current and future applications may benefit from the modification of the material properties by ion irradiation; some possibilities that have been already realized are summarized in the review in ref 5. The pronounced drive to nanoscaled structures in science and technology means that structure sizes of interest are now in the order of typical ion ranges of tens to hundreds of nanometers. This has led to several specific investigations into the ion–nanostructure interaction itself (e.g., for free-standing nanostructures, see refs 6–10) and to the advent of software to simulate their interactions (e.g., the code used for this work “iradina”<sup>11</sup> and others<sup>12</sup>).

The present work shows that the morphology of nanowires can be tuned by ion irradiation. Besides controlled bending,<sup>13</sup> we will demonstrate in this work that for certain ion implantation parameters (energy, fluence, direction, and temperature) nanostructures can be either only thinned by

sputtering, or also plastically deformed. Furthermore, through comparison with simulations and other studies,<sup>6–8,10,14–18</sup> the investigation of the nanostructure-size dependent behavior can reveal properties of the ion–material interaction in general. As their size is typically similar to ion ranges, nanowires are a suitable template to investigate the ion–material interaction in experimental arrangements not possible with bulk irradiation targets. Decreasing the nanostructure size, for example, limits the volume of material an energetic ion can interact with, regardless of the ions energy. Thus, the extent of the ion range and collision cascade can be probed indirectly by investigating diameter dependent sputtering in nanowires.

Top-down fabricated Si nanowires of various diameters were irradiated with multiple ion fluences at 300 °C while rotating at 45° to the ion-beam of 300 keV Ar<sup>+</sup>. Scanning electron microscopy (SEM) images shown in Figure 1a were taken of individual nanowires before and after each irradiation step. Image processing yields the diameter over height profile shown. Respective calculations (see Supporting Information) finally extract the diameter-dependent sputter yield for many nanowires (triangles in Figure 1b). The error bar indicates the standard deviation of the measured sputter yields of

**Received:** February 2, 2015

**Revised:** April 24, 2015

**Published:** May 7, 2015

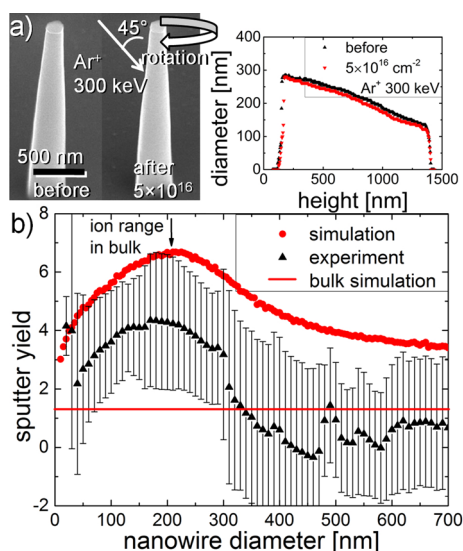


**Figure 1.** (a) Exemplary SEM images of a Si nanowire before and after  $5 \times 10^{16} \text{ cm}^{-2}$  ion irradiation. Irradiation conditions were 300 keV  $\text{Ar}^+$  at 300 °C and rotated at 45° between the nanowire axis and the ion beam. Such SEM images are analyzed to yield diameter over height profiles such as the one shown. From these profiles, the sputter yield as a function of diameter can be calculated for many nanowires. (b) Sputter yield of Si nanowires as a function of the diameter obtained by simulating the irradiation with 300 keV  $\text{Ar}^+$  with iradina (red circles). The indicated ion range of 300 keV  $\text{Ar}^+$  in Si-bulk at 45° is calculated with SRIM, the bulk sputter yield (red line) with iradina. The measured data-points (black triangles) correspond to the average of hundreds of individual measurements grouped together every 10 nm, and the “error bars” indicate the standard deviation. The outliers and discontinuities in the measured data curves at 40, 300, and 500 nm correlate with a low number of evaluated nanowires for those diameters and the change from one nominal diameter on the samples to another.

hundreds of individual measurements grouped together. Next to the experimental data points, simulation results are shown. The homogeneous irradiation of Si cylinders of varying diameters was implemented in the open source Monte Carlo simulation code iradina.<sup>11</sup> The sum of all atoms leaving the simulated volume per ion is plotted over the diameter of the nanowire (circles in Figure 1b). Similar results for 100 keV  $\text{Ar}^+$  irradiation are given in the Supporting Information.

The measured sputter yields reproduce the simulated diameter dependency qualitatively, albeit at a lower absolute value. The general behavior can be understood by regarding the collision cascade of an energetic ion of fixed energy and its interaction with nanowires of varying diameter. In nanowires with large diameters, atoms can only be sputtered from the surface facing the ion beam. Due to the cylindrical shape of the wires the angle of incidence is averaged over all angles smaller than the angle between the ion beam and the wire axis. The sputter yield thus converges to a value larger than the bulk sputter yield (red line in Figure 1a) even in the limit of infinite diameters.<sup>19</sup> At the other extreme, for a fixed energy for very thin wires the ions traverse through the wire and do not deposit all their energy in the wire, leading to low sputtering for small diameters. Starting at small diameters, increasing the diameter increases the total energy in the collision cascade and simultaneously also the surface area of the nanowires overlapping with the collision cascade. Therefore, the sputter yield quickly increases with diameter at small diameters. A clear

maximum in the sputter yield is seen when the diameter of the nanowire is comparable to the ion range at this energy, as calculated with the program “Stopping and Range of Ions in Matter” (SRIM)<sup>1</sup> (indicated in Figure 1b). For the fixed ion energy and this diameter the overlap of the distribution of the recoils and the nanowires surfaces is largest. This relation between particle size, ion range and sputtering is general to nanostructures, for example, a detailed analysis of the similar scenario of spherical nanostructures is made in ref 7 and more recently also for nanowires ref 6.

Some limitations have to be discussed if these simulation results are compared with experiments. On the theoretical side, the Sigmund sputter theory<sup>20</sup> defines a surface binding energy (SBE) and considers all recoils sputtered if they traverse the surface with an energy larger than the SBE in the projection onto the local surface normal. The SBE is conventionally set to the enthalpy of sublimation in the present case for Si to the bulk value of 4.7 eV.<sup>6,7</sup> The limitations of this approximation are already discussed in the original publication.<sup>20</sup> The accuracy with which Monte Carlo (such as SRIM,<sup>1</sup> iradina,<sup>11</sup> SDTrimSP<sup>21</sup> and TRIDYN<sup>22</sup>) codes can quantitatively predict sputtering depends on the correct SBE and the correct interaction potential between the atoms and ions within the target, especially at low collision energies.<sup>21</sup> Experimental results comparable to simulations can be obtained.<sup>23</sup> On the experimental side, native oxide formed<sup>24,25</sup> on the surface of the nanowires while they are exposed to air between irradiation and SEM analysis also has to be sputtered away. Thus, the net Si sputter yield will be systematically underestimated. However, the nanowires remain crystalline throughout the irradiation, as the amorphization threshold for 300 keV  $\text{Ar}^+$  in Si is arbitrarily large for temperatures >300 °C.<sup>26</sup> Electron backscattering diffraction (EBSD) images were made to confirm that the samples irradiated at 300 °C remained crystalline and those irradiated at room temperature were amorphized (see Supporting Information).

Silicon nanowires were also irradiated at room temperature and otherwise similar conditions (rotated, 45° angle, 100 keV  $\text{Ar}^+$ ). In this case not only sputtering, but also a change in the overall morphology of the nanowires was observed. Figure 2 shows the diameter of a single nanowire plotted over the height before and after  $1 \times 10^{16}$ ,  $3 \times 10^{16}$  and  $5 \times 10^{16} \text{ cm}^{-2}$  irradiations. Now the Si nanowires’ behavior is completely

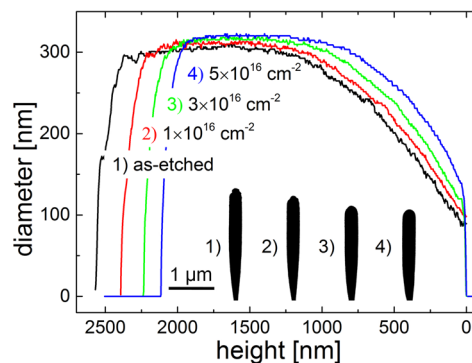


**Figure 2.** Diameter versus height of one single nanowire before (1, black-line) and after  $1 \times 10^{16}$  (2, red),  $3 \times 10^{16}$  (3, green) and  $5 \times 10^{16} \text{ cm}^{-2}$  (4, blue) 100 keV  $\text{Ar}^+$  irradiation. The clear shrinking and slight broadening are visible in both the plotted diameter profiles and the inset SEM profiles of this particular nanowire.

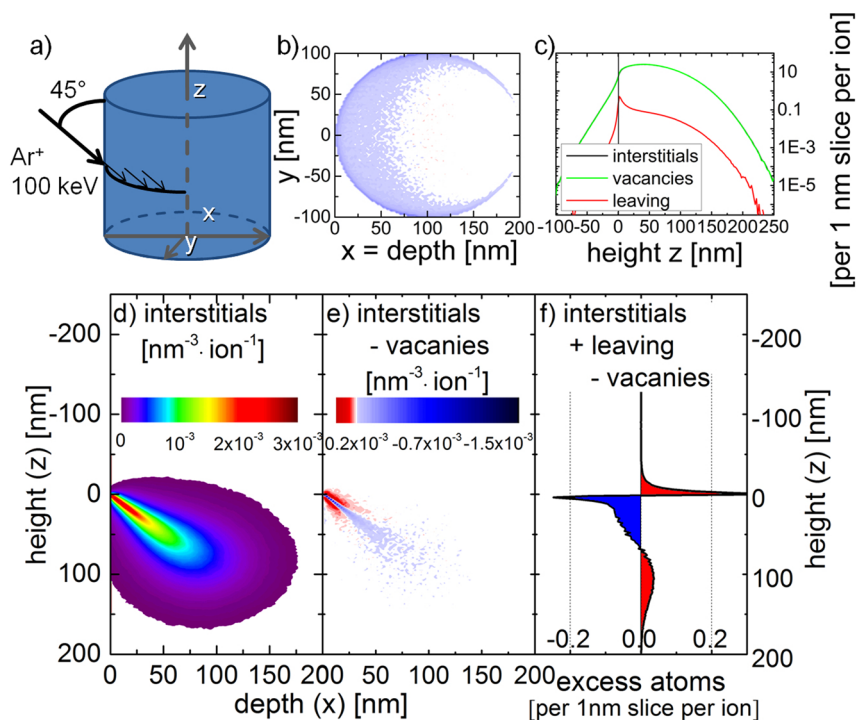


**Figure 3.** In the irradiation simulated with *iradina*, 100 keV  $\text{Ar}^+$  ions hit the 200 nm thick Si-NW at height zero and at an angle of  $45^\circ$ , as shown in (a). Interstitials per  $\text{nm}^{-3}$  and ion are plotted in (d) for an axial cross-section running through the middle of the nanowire. In (e), the difference of interstitials and vacancies is shown for the same cross-section with the excess of vacancies in blue and interstitial excess in red. The radial cross section in (b) shows this difference summed up over all heights. The prevalence of vacancies near the surface is a result of sputtering. The height profile of the vacancies subtracted from the sum of sputtered atoms and interstitials is plotted in (f). Because of mass conservation, summing up the profile over all heights yields zero. A strong oscillation around the impact-point accompanies a clear excess of vacancies at heights  $< 50$  nm and of interstitials around 100 nm. (c) The individual height profiles of interstitials, vacancies, and leaving atoms in a logarithmic plot; note that lines of the vacancies and interstitials overlap.

different than before, as they deform plastically during the irradiation. Instead of being thinned by sputtering, the nanowires shrink dramatically and become slightly thicker. The geometrical change is large and permanent and thus deemed to be plastic deformation. The profiles of this wire are also shown in the inset of Figure 2. They are obtained from the image analysis protocol (further details and SEM images in the Supporting Information).

A quantitative evaluation of this plastic deformation from such curves was performed to extract an effective mass-transport rate. This is a measure for the deformation which can directly be compared to simulation results. The method and results from this evaluation of 21 different nanowires are summarized in the Supporting Information. The average mass transport rate is  $1.2 \times 10^4$  atoms·nm/ion with a standard deviation of  $7 \times 10^3$  atoms·nm/ion, including some outliers with very large deformation. This means that in order to change the form of the nanowire from 1 to 2 (in Figure 2), on average  $1.2 \times 10^4$  atoms are displaced by one nanometer for every incoming ion.

We compare this result with a simulation using *iradina*.<sup>11</sup> Generally, there will be an inhomogeneous distribution of interstitials and vacancies left after a collision cascade has propagated through matter. The displacement of atoms has a preferential direction in line with the impinging ions momentum. An atom knocked-on leaves a vacancy earlier in the ions path to become an interstitial later. This could cause the plastic deformation, as an excess of interstitials can be understood as a local increase in density, and an excess in

vacancies can be a local decrease in density. This is especially true in amorphous materials for which it is not trivial to define what constitutes a point defect. Because it is reasonable to assume that the density of amorphous silicon is not changed dramatically by the irradiation,<sup>27</sup> in nanowires the strain caused by the different local densities may relax by plastic widening and shrinking. Effectively, mass is transported “downstream” along the ion beam, and the shape of the wire is changed. The magnitude of the mass-transport by knock-on in binary collisions can be estimated with the following simulation: A cylindrical Si nanowire of 200 nm diameter is irradiated at an angle of  $45^\circ$  to the nanowire axis with  $4 \times 10^6$   $\text{Ar}^+$  ions at 100 keV, as shown in Figure 3a. All  $\text{Ar}^+$  ions hit the nanowire at the same height  $z = 0$ , but at all possible lateral positions along  $y$ . The simulated volume is implemented in *iradina* as a 600 nm long cylinder with a diameter of 200 nm, divided into  $2 \times 2 \times 2$  nm voxels. In Figure 3d, the calculated number of interstitials is plotted for the axial cross-section through the wire. This is in principle a measure for the nuclear energy-loss and the average ion path can be clearly seen in the profile. The difference between interstitials and vacancies is shown in Figure 3e. The visualization is dominated by the excess of vacancies (shown in blue) on the plane running at  $45^\circ$  to the nanowire axis, coincident to the direct beam path. There is an excess of interstitials (in red) immediately above and below this plane due to the high probability of collisions between the impinging ion and a target atom with a high impact parameter. Such collisions change the impinging ion’s momentum only slightly and displace lattice atoms almost perpendicularly to the ion’s



path. Those recoils, which end up in the plane of incidence, are recombined with vacancies from an ion hitting the wire at other lateral positions. Further along toward the center of the simulated volume the difference between vacancies and interstitials is more diluted as the cascades have spread out due to lateral straggling. Figure 3b shows a radial cross section ( $x$ - $y$  plane), where the difference between interstitials and vacancies was summed up over all heights ( $z$ ). Near the impact line (surface) vacancies dominate, as the recoiled atoms here are likely to leave the simulated volume and contribute to sputtering. Further to the center of the wire a slight excess of interstitials is caused by the preferential knocking-on of recoils in the direction of the ion beam.

Figure 3f shows the height profile of the vacancies subtracted from the sum of interstitials and leaving atoms. The integral over this height profile has to be zero, as a displaced atom, which leaves behind a vacancy, can only become an interstitial or leave the volume entirely (i.e., be sputtered). Figure 3c illustrates that the total number of interstitials and vacancies per ion and 1 nm slice is 2 orders of magnitude larger than the difference between interstitials and vacancies. The number of vacancies and interstitials is very sensitive to the displacement energy. Its value is not well-defined for amorphous materials and was thus set arbitrarily to a reasonable value for crystalline Si, 15 eV.<sup>28</sup> The difference between vacancies and the sum of interstitials and leaving atoms (Figure 3f) is not affected by this value significantly. Low energy displacements ( $\leq 15$  eV) neither travel very far, nor with a preferential direction. The distribution of the leaving atoms (i.e., sputtering) looks as expected, with most atoms directly sputtered near the impact point. Almost all sputtered atoms originate from the surface voxels (see Figure 3b,c), indicating that they did not travel a long distance and are dominated by low energy collisions. The difference of the sum of interstitials and vacancies tallies where the displaced atoms are going. In effect, this is akin to recombination and it produces the local excess interstitials and vacancies. The strong oscillation near the impact height ( $z = 0$ ) is caused by the layers of interstitials and vacancies immediately around the ion beam.

The apparent mass-transport from the impact point downward can be quantified and compared to the plastic deformation seen in the experiment. The plot of the excess of vacancies or interstitials is weighted with the distance along the nanowire axis ( $z$ ), or the height of the slice in Figure 3f and summed over all heights ( $z$ ). This analysis yields  $78 \pm 1$  atoms·nm/ion. The effective mass-transport rate is on average one atom moving around 80 nm down the nanowire axis per ion impinging. This is more than 2 orders of magnitude less than the mass-transport rate which was estimated above from the experiments to be around  $1.2 \times 10^4$  atoms·nm/ion. It clearly shows that the knock-on mass-transport during irradiation, as simulated by binary collisions, cannot account for the plastic deformation of ion irradiated Si at room temperature.

To evaluate whether the plastic deformation is coincident with the ion beam direction, an individual nanowire was attached to a sharpened Au microwire with a focused ion beam (FIB) to allow irradiation from “below the substrate”. Figure 4a illustrates the principle, whereby the VLS-grown Si nanowire on an Au microwire, is fixed to a rotatable stage in the irradiation chamber under “ $-45^\circ$ ” to the ion beam. An illustration of the sample fabrication can be found in the Supporting Information. If the plastic deformation is orientated with the direction of the ion beam, as the binary collision

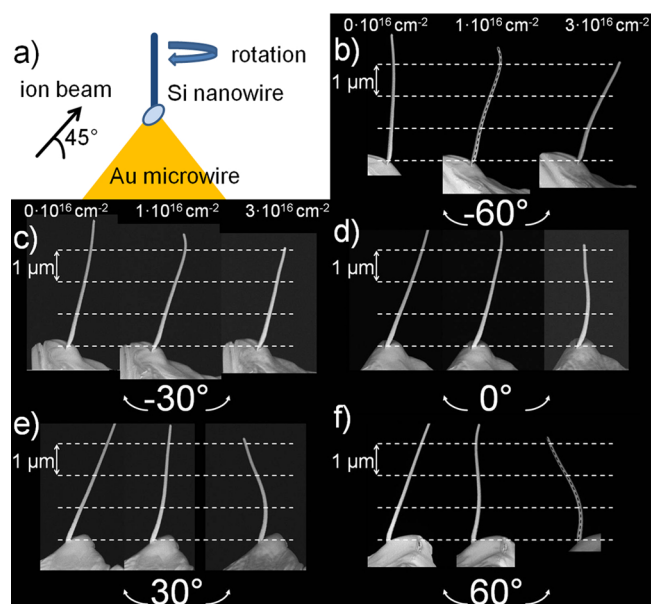


**Figure 4.** (a) Schematic illustration of the rotated irradiation under “ $-45^\circ$ ” to the nanowire axis. (b–f) SEM images acquired perpendicular to the axis of rotation during the irradiation. The same nanowire is shown at different observation angles shown below the respective images. The total irradiated fluence is indicated above the respective images in panel b,c. The angle of incidence of the ion beam is indicated on both sides of each image. The dashed horizontal lines are  $1 \mu\text{m}$  apart and guide the eye, while the dashed lines along the nanowires in panels b,f indicate where the length of these wires was measured.

simulation would suggest, then the nanowires would elongate under such irradiation conditions.

Figure 4b–f shows SEM images of one nanowire irradiated with 100 keV  $\text{Ar}^+$  ions while being rotated around an axis tilted at  $45^\circ$  to the ion beam. The SEM images are taken at the indicated observation angles of the same wire after the indicated total irradiation fluence. Because of shadowing of the ion beam by the supporting Au microwire and imperfect alignment of the nanowire axis and the axis of rotation, some bending of the wire is observed.<sup>13</sup> The unirradiated wire is straight and  $3.9 \mu\text{m}$  long (left SEM image in Figure 4b–f). The same wire after irradiation with  $1 \times 10^{16} \text{ cm}^{-2}$  is shown in the central SEM images. Its length was measured using Figure 4b, where it is presumed that the curvature is most in plane with the image (compare to 4e). A fifth order polynomial was fitted to the bent shape of the wire to obtain the full length of the wire at  $3.5 \mu\text{m}$ . The same was done after  $3 \times 10^{16} \text{ cm}^{-2}$  (right images) in 4f (compare to 4c) to obtain  $3.2 \mu\text{m}$ . Clearly, the wire shrank under the ion beam irradiation even though the projection of the ion beam was along the wire toward an unconstrained end.

The pertaining issues to the deformation and sputtering results can be best discussed in the context of the available simulation tools and models. Monte Carlo (MC)-based simulations generally rely on the binary collision approximation (BCA), which essentially neglects all collective atomic movement and thermal effects. They have been tremendously successful through the widespread use of the SRIM<sup>1</sup> code and its general and generally accurate prediction of stopping powers and thus ion ranges in matter. This is the basis for the iradina code used for the simulations in this work. These tools can be used to predict doping concentrations, nuclear, and electronic

energy losses, and so forth. They do not include the (thermal) movement of all individual particles. The energy-loss obtained from such calculations can be used in a second step to follow the thermal evolution locally, but not on an atomistic level. Without going into the details of various “thermal-spike” models here (for a review see ref 29), the energy-loss by the ion can be translated into a local temperature. This approach was used, for example, to develop a convincing viscoelastic model for the plastic flow of amorphous solids under swift heavy ion bombardment seen for ion energies much larger than 1 MeV.<sup>15</sup> This model relies on the assumption of a continuous, intensely excited region of cylindrical shape along the ion path to derive a deformation rate per fluence. It can explain why plastic deformation is not seen in crystalline materials, as the long-range order of the crystal structure is reimposed on the implanted area, reversing any deformation. Plastic deformation of silica particles has indeed been reported and compared to the viscoelastic model for silica nanoparticles irradiated with 300 keV Xe<sup>+</sup> ions.<sup>10</sup> Although the results reported here and those of ref 10 seem in line with the viscoelastic model,<sup>15</sup> the interpretation of what constitutes a thermal-spike is contentious. The total energy loss for 100 keV Ar<sup>+</sup> in Si is  $dE/dx = 36$  eV/nm of which the electronic energy loss is roughly half. Similarly, 300 keV Xe<sup>+</sup> in silica (ref 10) has an energy loss of  $dE/dx = 120$  eV/nm of which the electronic loss constitutes only 20%. The threshold for the electronic energy loss for the thermal-spike model is, however, given as  $dE/dx \geq 1$  keV/nm.<sup>15</sup> It seems therefore that this generalized model based on electronic energy loss derived from MC simulations is not applicable.

The main simulation alternatives are molecular dynamics (MD) codes, which model each atom individually and thus could also solve temperature-related phenomena. The difficulty here is treating electronic energy-loss consistently and finding the right interaction potential for the particles in the investigated scenario. Beside these difficulties, there have been successful comparisons of sputter yields of Au nanoparticles irradiated with 80 keV Xe investigated with in situ transmission electron microscopy and MD simulations.<sup>8</sup> Also MD simulations performed on Si and metals suggest the formation of nanoscale “liquid” pockets in the self-irradiation at 10 keV.<sup>16</sup> A recent MD study predicts plastic deformation in metallic glasses irradiated by high energy neutrons due to cascades initiated by primary knock-on atoms.<sup>18</sup> The collision cascades in that study were induced by 475 keV Nb primary knock-on atoms in *a*-Cu<sub>50</sub>Nb<sub>50</sub>. This atomistic model explicitly shows that the same process of local expansion and stress relaxation, as it is described by the viscoelastic model by Trinkaus et al.,<sup>15</sup> can also occur in collision geometries with less symmetry and that it can be induced by nuclear energy-loss. Contrasting this, a MD study by Mayr et al.<sup>17</sup> on 10 eV to 100 keV recoils of Cu and Ti in *a*-CuTi came to the conclusion that the viscous flow is dominated by the effect of ion induced point defects, although here only the relaxation of stress is investigated, not the combination of creation and relaxation.

The results from the present study show that the BCA is valid in describing the propagation of Ar<sup>+</sup> in Si at moderate energies. The qualitative agreement between experiment and BCA simulation on the diameter dependent sputtering supports the correct reproduction of the collision cascades by the BCA. The irradiation at 300 °C shows that there is no plastic deformation at elevated temperatures. The full recrystallization after each ion impact reimposes a long-range order on the local

strained region of the collision cascade, reversing any local deformation. Even though the temperature is elevated and thermal effects are presumably enhanced, the BCA-simulation is able to predict the diameter dependent sputter yield within the experimental accuracy. As sputtering is a measure of the overlap of the nanostructure surface and the recoil distribution, it probes the geometry of the collision cascade. Agreement between simulation and experiment thus shows the general validity of the BCA and its usefulness in a first approximation of the ion–nanostructure interaction. Sputtering may be underestimated by the simulation as ejection of clusters can not be simulated in the BCA. An estimation of cluster sputtering was also made in refs 6 and 7 but unfortunately the MD simulations required to address this issue can not yet encompass structures as large as the ones investigated here. Even though the BCA simulation very well predicts the presence of a maximum in the sputter yield at a diameter corresponding to the ion range, the slight shift of the measured maximum sputter yield toward lower diameters suggests that thermal effects may influence sputtering.

The deformation observed after room-temperature irradiation is not directed along the impinging ions inertia, as it leads to a contraction of the wires regardless of the direction of the ion beam. A model considering the local excess of interstitials and vacancies by knock-on mass-transport based on BCA simulations fails with regard to the magnitude and direction of this effect. Clearly, a predictive model will have to consider a “thermal spikelike” process although the classical “thermal spike” regime is not reached by far. The specific geometrical constraints are much more complex with nanostructured samples and low energy (and thus low-symmetry) collision cascades than in the known swift-heavy ion induced deformation modeled by Trinkaus<sup>15</sup> and others. Nevertheless, there is the possibility of an analogous process taking place even though there is no cylindrical thermal spike of heated material. The MD simulations of ref 18 show that in a collision cascade that extends elliptically there can be a contraction parallel to the long axis and an expansion in the shorter axes. The reason for this is that an ellipsoidal collision cascade tends to become more spherical under the internal pressure of the atoms heated by the deposited energy. In Figure 3e, it can be clearly seen that for the irradiation of Si with 100 keV Ar<sup>+</sup> an elongated ellipse is the most probable geometry for the collision cascades. Figure 5a shows that the material affected by the collision cascade is heated and that the ellipsoidal form of the collision cascade results in an anisotropic expansion and plastic deformation of the material around the collision cascade. If the density before and after the irradiation is the same, then the relative expansion perpendicular to the ion beam is equal to half the relative compression parallel to it. Multiple such deformations can be added to form the straining field shown in Figure 5b with a net plastic deformation without a change in volume, if  $-2\varepsilon_{\perp} = \varepsilon_{\parallel}$ . For the viscoelastic model of ref 15, a similar approach is taken. As the nanowire is rotated under the ion beam, the shearing components in the deformation cancel when the coordinate system is changed to the one in Figures 3a and 5c with the ion beam at 45° to the nanowire axis. Then the deformation  $\varepsilon_{zz}$  parallel to the nanowire axis averages out to half the deformation along the ion beams path  $\varepsilon_{zz} = 1/2\varepsilon_{\parallel}$ . This is independent of whether an angle of –45° or 45° is used because they are symmetrical. Thus, a contraction of material parallel to the ion beam would lead to the shrinking of the nanowires observed in the experiment. The strain rate can also

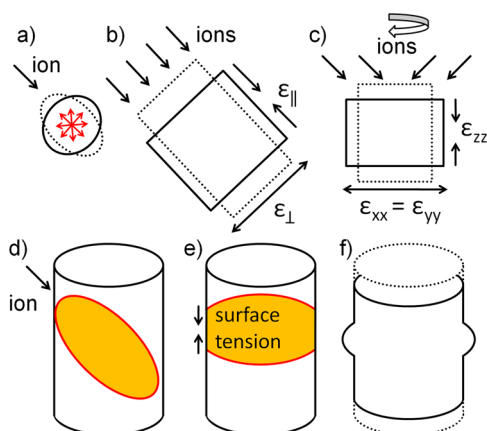


**Figure 5.** (a) Illustration of the pressure induced anisotropic deformation of the material in and around a single collision cascade (based on ref 18); the dotted lines show the shape before irradiation. The sum of many such deformation events can be summarized as a straining field shown in (b). The straining parameters are  $\epsilon_{\perp}$  and  $\epsilon_{\parallel}$  perpendicular and parallel to the ion beam, respectively. In the rotated coordinate system with the z-axis parallel to the nanowires axis shown in (c), the average of all such straining fields oriented along the respective ion beam directions yields  $\epsilon_{zz}(xx,yy) = 1/2\epsilon_{\parallel}(\epsilon_{\perp})$ . The alternative model is shown schematically in (d–f). The volume of material heated by the ion beam is comparable to the extent of the nanowire in (d) (compare also Figure 3d). This reduces the viscosity of the material locally and allows surface tension driven, viscous flow of material shown in (e) to reduce the surface energy by increasing the local radius to form (f).

be quantified roughly from the experimental data by evaluating the height change per fluence linearly, yielding  $2(d\epsilon_{zz}/d\Phi) = d\epsilon_{\parallel}/d\Phi = 6 \times 10^{-18} \text{ cm}^2/\text{ion}$  or 6% strain per  $10^{16} \text{ ions/cm}^2$  with a large standard deviation of  $6 \times 10^{-18} \text{ cm}^2/\text{ion}$ . This value is more than an order of magnitude smaller than the deformation of  $10^{-16} \text{ cm}^2/\text{ion}$  of 300 keV Xe in silica nanoparticles reported in ref 10 and more than 2 orders of magnitude smaller than the MD result of  $10^{-15} \text{ cm}^2/\text{ion}$  of ref 18. A problem with this model is that there is no reason why this plastic deformation should not be seen in bulk, yet there are no reports of plastic straining in bulk Si. A straining rate of 6% strain per  $10^{16} \text{ ions/cm}^2$  in a layer of  $\sim 300 \text{ nm}$  would be sufficiently large to be measurable in experiments on the bending of thinned Si wafers similar to refs 14 and 30. A further, major concern with applying this model to nanostructures stems from the interaction with the local environment. In the MD investigation, the collision cascade is enveloped in bulk material with an isotropic temperature and pressure background. In a nanostructure, there is not much material around and it is not distributed around the cascade in an isotropic way.

This leads to an alternative driving force for the plastic deformation: surface tension. Illustrated in Figure 5d, an impinging ion depositing its energy close to the surface can heat the material to lower the viscosity and enable normal viscous flow. The reduced viscosity is not fully reliant on an increased local temperature, as ion-induced lowering of the viscosity has been observed previously<sup>17,31,32</sup> and will also contribute. The MD simulations of refs 16 and 18 suggest that the energy density (corresponding to temperatures close to  $T_{\text{melt}}$ ) and distribution (tens of nanometers) are large enough to significantly affect nanowires. A tentative indication that the material becomes viscous under ion bombardment can be seen in the characteristic rounding and smoothing of the wires'

surface seen in the cross sections of the wires after irradiation shown in the inset of Figure 2 and the SEM images of irradiated wires in Figure 4 and in the Supporting Information. The wires look as though they were molten. Figure 5e,f shows that as the surface energy scales inversely with the squared radius there is a driving force for material to bulge outward, increasing the radius and decreasing the height of the wire. This effect is independent of the irradiation angle.

In summary, a surface tension driven plastic deformation under low energy ion bombardment is the most likely explanation for the observed results. This illustrates that the behavior of nanostructured materials can deviate significantly from the bulk behavior, where no such deformation is observed. The large surface to volume ratio is key to the relevance of the surface tension to material properties and in nanostructures this ratio is greatly enhanced. In addition to the enhanced sputtering, the plastic deformation will have to be considered when irradiating nanostructures of Si and also other materials. It may even turn out to be an asset in the emerging field of MEMS devices based on nanostructured Si as a tool to fabricate strained devices. Investigations, where the plastic deformation described here may be relevant, include the formation and manipulation of nanopores,<sup>33</sup> bending of nanowires,<sup>34,35</sup> and the manipulation of free-standing films.<sup>9,36</sup> It is also relevant to the controversial issue of nanoripple formation on ion irradiated Si surfaces, as it is still debated with respect to the influence of curvature and angle dependent sputtering,<sup>37</sup> and ion induced strain and mass-transport.<sup>38,39</sup> The ion-induced deformation shown in this work shows some similarity to the viscous flow shown by Kramczynski et al. in ref 39, further indicating that a detailed atomistic investigation may have to be considered to form an extensive ripple formation model.

We have shown that the seemingly simple irradiation of Si with  $\text{Ar}^+$  at two different temperatures can reveal a lot of information on the principle ion–mater interaction. If anything, then the ion irradiation of Si has been investigated extensively. Nevertheless, new effects can be revealed for the nanostructured material, which has fewer geometrical constraints. The geometrical constraints directly influence sputtering as expected and with good agreement to independently published predictions.<sup>6</sup> However, the irradiation of nanostructured Si reveals a previously unknown plastic deformation of Si under low energy ion irradiation. Also we show that BCA simulations are successful at predicting the extent of the collision cascades and thus the qualitative behavior of sputtering. It is clear, however, that the evolution of a nanostructure under ion irradiation is more complex than just the collision cascade effects. The full reality includes, for example, stress, viscous flow, thermal effects, density relaxation, and so forth, and all these effects are beyond the scope of such simulation programs. The BCA simulations are a useful prerequisite for further investigations into other effects and the discrepancy between the mass-transport simulation and experimental results is intended as a warning against their naive use, not as fundamental criticism of it.

**Methods.** The Si nanowire arrays used in the first part of this study were made using a top-down process by inductively coupled plasma reactive ion etching (ICP-RIE) at cryogenic temperatures. E-beam lithography, e-beam evaporation, and lift-off was used to define a hard-mask with an array of circular Ni pads of varying diameter onto a Si [111] wafer. The patterned samples were then loaded into the RIE system and cooled to  $-108^\circ\text{C}$ . Etching of the samples was done with a set pressure



of 10 mTorr and a strike pressure of 30 mTorr. RF and ICP powers were set to 15 and 100 W, respectively. Gas flow rates of 50 sccm  $\text{SF}_6$  and 100 sccm  $\text{O}_2$  were used. The samples were etched for 5 to 15 min. After RIE processing, the Ni hard mask was removed using 32% HCl and a (7:1)-buffered HF dip was done to remove the native oxide of Si from the surface. Nonideal  $\text{O}_2$  flow rates caused inhomogeneous lateral etching rates leading to tapered wires, typically with a rounded triangular cross-section corresponding to the higher Si {100} etching rates.

For the irradiation under angles of “ $-45^\circ$ ” between the wire axis and the ion beam, Si wires grown epitaxially on a Si[111] wafer via vapor–liquid–solid (VLS) process were used. The nanowires were grown in an LPCVD reactor with Au colloids dispersed on the substrate as catalyst. A growth pressure of 3 mbar at  $515^\circ\text{C}$  under monosilane/hydrogen atmosphere leads to <111>-oriented nanowires as described in ref 40. Such Si nanowires of  $\sim 100$  nm diameter were transferred onto the tips of Au wires with a diameter of  $\sim 25\ \mu\text{m}$  using the micromanipulation tool, e-beam Pt-deposition and ion beam milling in a FEI Dual-Beam FIB system (Supporting Information).

All irradiations were performed on a rotatable, heatable, and tilted stage within an ion implanter. The array samples were irradiated up to a total fluence of  $5 \times 10^{16}\ \text{cm}^{-2}$   $\text{Ar}^+$  in three steps,  $1 \times 10^{16}\ \text{cm}^{-2}$ ,  $2 \times 10^{16}\ \text{cm}^{-2}$ , and  $2 \times 10^{16}\ \text{cm}^{-2}$  at 100 and 300 keV with an ion flux of less than  $2 \times 10^{16}\ \text{cm}^{-2}\ \text{h}^{-1}$ . These irradiations were done at an angle of  $45^\circ$  between the ion beam and the substrate normal, while rotating the sample at around 50 rpm. The irradiations were performed at  $300^\circ\text{C}$  and room temperature.

Samples were investigated before and after each irradiation with a high-resolution SEM in the Dual-Beam FIB system. The resolution of this system can be estimated to around 2 nm. Images were made at an angle of  $45^\circ$  to the substrate normal and aligned to the nanowire arrays. For the reproducible quantitative analysis of the wires, after each irradiation step a semiautomated image analysis protocol was followed (Supporting Information).

## ■ ASSOCIATED CONTENT

### ■ Supporting Information

The Supporting Information contains details on the method used to quantify the sputter yield and mass-transport-rate from SEM images. It also contains further SEM images of the plastically deformed nanowires, EBSD diffractograms of the room-temperature and  $300^\circ\text{C}$  irradiated wires, and an illustration of a nanowire glued to a microwire in a FIB dual-beam system. The Supporting Information is available free of charge on the ACS Publications website at DOI: 10.1021/acs.nanolett.5b00431.

## ■ AUTHOR INFORMATION

### Corresponding Author

\*E-mail: andreas.johannes@uni-jena.de.

### Notes

The authors declare no competing financial interest.

## ■ ACKNOWLEDGMENTS

The authors gratefully acknowledge financial support by the Austrian Science Fund (FWF): project No. I 724-N16. We gratefully acknowledge the financial support of the Deutsche

Forschungsgemeinschaft (DFG) within the D-A-CH Project “wiring quantum dots” Ro 1198/14-1 and Grant INST 275/241-1 FUGG, and the Thüringer Ministerium für Bildung, Wissenschaft und Kultur (TMBWK), Grant 62-4264-925/1/10/1/01. We also want to acknowledge the referees for their valuable comments during review and Professor W. Möller and E. Schmidt for helpful discussions.

## ■ REFERENCES

- (1) Ziegler, J. F.; *The stopping and range of ions in solids*; Pergamon Press: New York, 1985; p 308–315.
- (2) Nastasi, M.; Mayer, J.; Hirvonen, J. K. *Ion-Solid Interactions: Fundamentals and Applications*; Cambridge University Press: Cambridge, 2008.
- (3) *Materials Science with Ion Beams*; Bernas, H., Ed.; Topics in Applied Physics 116; Springer: Berlin, 2010.
- (4) Schmidt, B. *Ion Beams in Materials Processing and Analysis*; Springer: New York, 2012.
- (5) Ronning, C.; Borschel, C.; Geburt, S.; Niepelt, R.; Müller, S.; Stichtenoth, D.; Richters, J. P.; Dev, A.; Voss, T.; Chen, L.; Heimbrodt, W.; Gutsche, C.; Prost, W. *Phys. Status Solidi B* **2010**, *247* (2329–2337), 00006.
- (6) Urbassek, H. M.; Bradley, R. M.; Nietiadi, M. L.; Möller, W. *Phys. Rev. B* **2015**, *91*, 165418.
- (7) Nietiadi, M. L.; Sandoval, L.; Urbassek, H. M.; Möller, W. *Phys. Rev. B* **2014**, *90*, 045417.
- (8) Greaves, G.; Hinks, J. A.; Busby, P.; Mellors, N. J.; Ilinov, A.; Kuronen, A.; Nordlund, K.; Donnelly, S. E. *Phys. Rev. Lett.* **2013**, *111* (065504), 00004.
- (9) Chalapat, K.; Chekurov, N.; Jiang, H.; Li, J.; Parviz, B.; Paraoanu, G. S. *Adv. Mater.* **2013**, *25*, 91–95.
- (10) Dillen, T. v.; Polman, A.; Kats, C. M. v.; Blaaderen, A. v. *Appl. Phys. Lett.* **2003**, *83*, 4315–4317.
- (11) Borschel, C.; Ronning, C. *Nucl. Instrum. Methods Phys. Res., Sect. B* **2011**, *269*, 2133–2138.
- (12) Möller, W. *Nucl. Instrum. Methods Phys. Res., Sect. B* **2014**, *322*, 23–33.
- (13) Borschel, C.; Spindler, S.; Lerose, D.; Bochmann, A.; Christiansen, S. H.; Nietzsche, S.; Oertel, M.; Ronning, C. *Nanotechnology* **2011**, *22* (185307), 00019.
- (14) Volkert, C. A. *J. Appl. Phys.* **1991**, *70*, 3521–3527.
- (15) Trinkaus, H.; Ryazanov, A. I. *Phys. Rev. Lett.* **1995**, *74*, 5072–5075.
- (16) Nordlund, K.; Ghaly, M.; Averback, R. S.; Caturla, M.; Diaz de la Rubia, T.; Tarus, J. *Phys. Rev. B* **1998**, *57*, 7556–7570.
- (17) Mayr, S. G.; Ashkenazy, Y.; Albe, K.; Averback, R. S. *Phys. Rev. Lett.* **2003**, *90*, 055505.
- (18) Baumer, R. E.; Demkowicz, M. J. *Mater. Res. Lett.* **2014**, *2*, 221–226.
- (19) Yamamura, Y.; Shindo, S. *Radiat. Eff.* **1984**, *80*, 57–72.
- (20) Sigmund, P. *Phys. Rev.* **1969**, *184* (383–416), 03204.
- (21) Eckstein, W. *Computer Simulation of Ion-Solid Interactions*; Springer: Berlin, Heidelberg, 1991.
- (22) Möller, W.; Eckstein, W. *Nucl. Instrum. Methods Phys. Res., Sect. B* **1984**, *2*, 814–818.
- (23) Hofsäss, H.; Zhang, K.; Mutzke, A. *Appl. Surf. Sci.* **2014**, *310*, 134–141.
- (24) Lukeš, F. *Surf. Sci.* **1972**, *30*, 91–100.
- (25) Al-Bayati, A. H.; Orrman-Rossiter, K. G.; van den Berg, J.; Armour, D. *Surf. Sci.* **1991**, *241*, 91–102.
- (26) Pelaz, L.; Marqués, L. A.; Barbolla, J. J. *Appl. Phys.* **2004**, *96*, S947–S976.
- (27) Hedler, A.; Klaumünzer, S. L.; Wesch, W. *Nat. Mater.* **2004**, *3*, 804–809.
- (28) Corbett, J. W.; Watkins, G. D. *Phys. Rev.* **1965**, *138*, A555–A560.
- (29) Wesch, W.; Kamarou, A.; Wendler, E. *Nucl. Instrum. Methods Phys. Res., Sect. B* **2004**, *225*, 111–128.

- (30) Massl, S.; Köstenbauer, H.; Keckes, J.; Pippan, R. *Thin Solid Films* **2008**, *516*, 8655–8662.
- (31) Snoeks, E.; Boutros, K. S.; Barone, J. *Appl. Phys. Lett.* **1997**, *71*, 267–269.
- (32) Hu, X.; Cahill, D. G.; Averbach, R. S. *J. Appl. Phys.* **2002**, *92*, 3995–4000.
- (33) George, H. B.; Tang, Y.; Chen, X.; Li, J.; Hutchinson, J. W.; Golovchenko, J. A.; Aziz, M. J. *J. Appl. Phys.* **2010**, *108*, 014310.
- (34) Cui, A.; Fenton, J. C.; Li, W.; Shen, T. H.; Liu, Z.; Luo, Q.; Gu, C. *Appl. Phys. Lett.* **2013**, *102*, 213112.
- (35) Romano, L.; Rudawski, N. G.; Holzworth, M. R.; Jones, K. S.; Choi, S. G.; Picraux, S. T. *J. Appl. Phys.* **2009**, *106*, 114316.
- (36) Kim, Y.-R.; Chen, P.; Aziz, M. J.; Branton, D.; Vlassak, J. J. *J. Appl. Phys.* **2006**, *100*, 104322.
- (37) Bradley, R. M.; Harper, J. M. E. *J. Vac. Sci. Technol., A* **1988**, *6*, 2390–2395.
- (38) Norris, S. *Phys. Rev. B* **2012**, *86*, 235405.
- (39) Kramczynski, D.; Reuscher, B.; Gnaser, H. *Phys. Rev. B* **2014**, *89*, 205422.
- (40) Lugstein, A.; Steinmair, M.; Hyun, Y. J.; Hauer, G.; Pongratz, P.; Bertagnolli, E. *Nano Lett.* **2008**, *8*, 2310–2314.